The effect of Fe on chemical stability and oxygen evolution performance of high surface area SrTi$_{x-1}$Fe$_x$O$_{3-\delta}$ mixed ionic-electronic conductors in alkaline media

Krystian Lankauf [a,*], *Aleksander Mroziński* [a], *Patryk Błaszczak* [b], *Karolina Górnicka* [b], *Justyna Ignaczak* [a], *Marcin Łapiński* [b], *Jakub Karczewski* [b], *Grzegorz Cempura* [c], *Piotr Jasiński* [a], *Sebastian Molin* [a]

[a] *Advanced Materials Center, Faculty of Electronics, Telecommunications and Informatics, Gdańsk University of Technology, Ul. G. Narutowicza 11/12, 80-233, Gdańsk, Poland*
[b] *Advanced Materials Center, Faculty of Applied Physics and Mathematics, Gdańsk University of Technology, Ul. G. Narutowicza 11/12, 80-233, Gdańsk, Poland*
[c] *International Centre of Electron Microscopy for Materials Science, AGH University of Science and Technology, Al. A. Mickiewicza 30, 30-059, Kraków, Poland*

HIGHLIGHTS

- High surface area SrTi$_{x-1}$Fe$_x$O$_{3-\delta}$ perovskites were prepared via a solid state reaction.
- The effect of Fe on electrical and physicochemical properties was investigated.
- Fe substitution increases activity toward OER.
- Chemical stability tests showed Sr dissolution for Fe content above 50%.

GRAPHICAL ABSTRACT

ARTICLE INFO
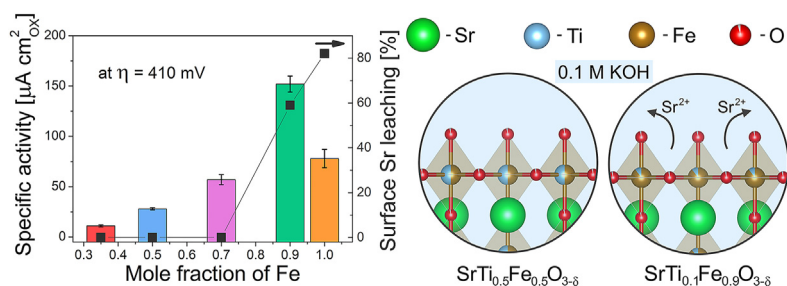
ABSTRACT

Development of environmentally friendly, high performing oxygen evolution reaction (OER) catalysts is an important research challenge. In this work, iron doped strontium titanates with a general formula SrTi$_{1-x}$Fe$_x$O$_{3-\delta}$ (x = 0.35, 0.50, 0.70, 0.90, and 1.00) denoted as STFx, were synthesized via a solid state reaction technique and characterized in terms of oxygen evolution reaction electrocatalysis in an alkaline electrolyte (0.1 M KOH). The produced powders were characterized by a high specific surface area (>20 m^2 g^{-1}), beneficial for OER. The evaluation of specific activity indicated the following trend of increasing performance: STF35 < STF50 < STF70 < SFO < STF90. The lowest overpotential at 10 mAcm^{-2} $_{GEO}$ of 410 mV (350 mV at 25 μA cm^{-2}$_{OX}$) was achieved by STF90 with the

Oxygen evolution reaction
Water splitting
Electrocatalysts
Chemical stability

corresponding Tafel slope of 60 mV dec^{-1}. The two materials with the highest Fe content (i.e. STF90 and SFO) showed, however, poor chemical stability in alkaline solution demonstrated by the dissolution of Sr. Based on the good electrochemical performance (~460 mV at 10 mA cm^{-2}$_{GEO}$, ~405 mV at 25 µA cm^{-2}$_{OX}$) and chemical stability for at least 30 days (no Sr dissolution) of STF50, it can be considered an interesting, working at room temperature OER catalyst based on non-toxic and abundant elements.

Introduction

Alkaline electrochemical water splitting is an important method for hydrogen production which can be used to accommodate an increasing share of renewable energy production [1,2]. The overall efficiency of water splitting is mainly determined by the sluggish oxygen evolution reaction (OER) kinetics. Precious metal oxides: RuO$_2$ and IrO$_2$, are known for superior OER activity, however, their low abundance and high price are a barrier against widespread use.

As potential alternative electrocatalysts, many different groups of materials have been researched, including especially oxides (perovskites [3–6] and spinels [7–10]), carbides [11–13], phosphides [14–16], and layered double hydroxides (LDHs) [17–19]. In recent years, highly active oxide electrocatalysts with the perovskite structure have been developed. Perovskites have a general formula of ABO$_3$ (where A is large rare earth or alkaline metal cation and B is a smaller, redox active transition metal cation) [20]. A wide range of element selection provides prospects of tailoring the physical and chemical properties, enhancing the catalytical activity [21,22]. Notable examples of the perovskites include especially cobalt and/or iron containing compounds. The high performance catalysts include: LSC, LSF, BSCF, SCF and their variations. For instance, Zhang et al. prepared series of perovskite-type oxide La$_{1-x}$Sr$_x$CoO$_3$ by sol-gel process [23]. La$_{0.2}$Sr$_{0.8}$CoO$_3$ exhibited the highest OER activity, which can be additionally tuned by changing the synthesis parameters, i.e. molar ratios of substrates, pH of the sol, calcination time and temperature. The OER performance of SrTi$_{0.1}$Co$_x$Fe$_{0.9-x}$O$_{3-\delta}$ in alkaline media studied by Deng et al. revealed the highest OER activity of SrTi$_{0.1}$Co$_{0.5}$Fe$_{0.4}$O$_{3-\delta}$ [24]. The improved electrochemical performance is considered to originate from the highly oxidative oxygen species O$_2^{2-}$/ O$^-$ formed upon moderate Fe doping. As demonstrated, the perovskites based on cobalt offer high electrochemical performance, although cobalt is proven to be a carcinogenic element with high price variations and ethical issues with mining. Due to the mentioned issues, substitution with the other elements is an active research topic in solid state chemistry.

Fe-based perovskites have been studied as potential alternatives for Co-based materials. Among the ferrites, the perovskites with B-site based on Ti and Fe have found considerable attention as model OER/ORR and hydrogen catalysts at high temperatures [25,26]. For example, SrFe$_{0.2}$, $_{0.3}$TiO$_{3-\delta}$ (SFT) and SrFe$_{0.2}$Ti$_{0.8}$O$_{3-\delta}$ (SFT)-ZnO composite heterostructure demonstrated high ionic conductivity at 520 °C and has been successfully applied as an electrolyte for low-temperature solid oxide fuel cell (LT-SOFC) [27,28]. Pure SrTiO$_3$ is a poor electronic conductor due to a stable Ti^{4+} cation, but upon partial substitution of Ti by Fe, the electronic conductivity increases and ionic conductivity is introduced via the formation of oxygen vacancies [29,30]. The opposite end member, Sr$_2$Fe$_2$O$_5$ (SrFeO$_{2.5}$), with the iron oxidation state of +3, can be treated as a highly oxygen deficient perovskite that crystallizes in an orthorhombic structure [31].

The compounds with both Fe and Ti at the catalytically active B-site show mixed ionic-electronic conductivity and high electrochemical performance, even though they have a relatively low electronic conductivity, especially compared to LSC or LSF perovskites [32,33]. The relations between the electronic conductivity, ionic conductivity, oxygen exchange and diffusion and stability are not yet well established at high temperatures, which also seems the case at low temperatures.

Sr(Ti,Fe)O$_{3-\delta}$ materials have been already considered as potential OER electrocatalysts. For example, Hayden et al. have used high throughput physical vapor deposition (HT-PVD) to deposit an array of 100 compositions with different Ti:Fe ratios for evaluation of OER/ORR [34]. The materials were prepared in the form of 300 nm thin films. The higher the Fe content was, the lower the OER onset potential was measured, whereby the stability showed an opposing trend. This developed screening study pointed out potentially interesting features of the Sr(Ti,Fe)O$_{3-\delta}$ materials for OER, which were, however, not carefully studied on well-defined powder catalysts in an RDE-setup and thus a direct comparison of their performance with other perovskites in the powder form is difficult.

In the present work, a series of SrTi$_{1-x}$Fe$_x$O$_{3-\delta}$ (x = 0.35, 0.50, 0.70, 0.90, and 1.00) (STFx) perovskites were prepared by the high temperature solid state reaction technique. The materials were examined for their crystallographic structure, chemical stability, electrical conductivity properties, and finally, the evaluation of the electrocatalytic OER activity in alkaline electrolyte (0.1 M KOH) at 25 °C was performed on a rotating disk electrode.

The main focus of our research was to investigate the influence of the Fe substitution on the chemical stability and electrocatalytic activity of SrTi$_{1-x}$Fe$_x$O$_{3-\delta}$ perovskites.

Experimental details

Material synthesis

Catalyst materials SrTi$_{1-x}$Fe$_x$O$_{3-\delta}$ (STFx) with x = 0.35, 0.50, 0.70, 0.90, and 1.00 were synthesized by a standard high

temperature solid state reaction method (HT-SSR). Starting materials were: strontium carbonate ($SrCO_3$), iron (III) oxide (Fe_2O_3) and titanium dioxide (TiO_2) with purity >99% (all from Sigma-Aldrich, USA). Reagents were mixed together in a planetary ball mill according to the details presented in the previous work [35,36]. The mixed reagents were calcined twice for 15 h in the form of large pellets ($\Phi = 1\ 1/8$", h $\approx$ 1.5 mm) with a re-grounding step between each calcinations. Due to the high sinter-ability of the $SrTi_{1-x}Fe_xO_{3-\delta}$ with x = 1.00, calcination temperature was set to 1100 °C, whereas for the remaining materials, the temperature peaked at 1200 °C. After the second calcination step, the pellets were ground into powders, milled in a ball mill (using 3 mm ZrO_2 balls in ethanol, Fritsch Pulverisette 7) and annealed in air at 600 °C to obtain oxygen stoichiometric powders [37].

For the specific surface area measurements, 1000 mg of powder was ball-milled for 96 h with the rotation speed of 100 rpm (Zoz Gmbh, Rollermill RM1) in 20 mm diameter glass vial of total 25 mL capacity filled with 35 g of 1 mm diameter yttria-stabilized zirconia (YSZ) grinding balls and 13 mL of ethanol. The reason of the ball-milling procedure was to mimic the catalysts' specific surface changes after ink ball-milling described further in the electrode preparation paragraph.

Dense STFx pellets for electrical measurements and chemical stability tests were prepared by uniaxial pressing at 50 MPa and sintering for 2 h at either 1100 °C (pure SFO) or 1200 °C (the remaining composition) under air atmosphere.

The chemical stability tests were performed by immersing the sintered pellets (~0.5 mm thick) in 0.1 M KOH solution (pH ~13) for 30 days. The samples' microstructures (SEM) and chemical compositions (EDS) were compared before and after the tests. For the tests, the pellets after the electrical conductivity tests were used. To reveal the grain boundaries, the surfaces of the sintered pellets were polished down to a ~1 μm finish and then thermally etched at 1200 °C for 5 min (except SFO: 900 °C, STF90, and STF35 at 1100 °C). An example of the thermal etching temperature selection procedure is described in Supporting Information (Figs. S1 and S2).

Material characterization

Synthesized powder morphologies were investigated using FEI Quanta 250 FEG Scanning Electron Microscope and a C_s-corrected Titan Cubed G2 60−300 (FEI) Scanning Transmission Electron Microscope (S/TEM). Chemical composition was examined using the ChemiSTEM EDX system based on four windowless Silicon Drift Detectors (Super X). The powders for TEM investigations were prepared traditionally: a drop of a water suspension containing the powder was placed onto a copper grid followed by vacuum drying. The maximum particle diameter was estimated, based on SEM images, using the ImageJ software [38].

Surface morphology and elemental composition of the pellets before and after exposures in 0.1 M KOH solution were investigated on a Phenom XL (Thermo Fisher Scientific)

desktop SEM equipped with an integrated energy dispersive X-ray spectroscopy (EDS) microanalyzer.

The powders' specific surface area was measured using N_2 adsorption technique (Quantachrome, NovaTouch LX1) according to the BET isotherm model. The samples were degassed prior sorption measurement at 300 °C for 3 h under vacuum.

Powder X-ray diffraction (pXRD) was conducted at room temperature on a Bruker D2 Phaser diffractometer with CuK_α radiation (λ = 1.5404 Å) and a Lynxeye XE-T detector was used for crystalline phase identification. Unit cell parameter calculation was performed by Le-Bail refinement using the Fullprof software package [39]. The .cif files were downloaded from the Crystallography Open Database [40,41].

The chemical composition of samples was investigated by the X-ray photoelectron spectroscopy (XPS) method. Measurement was performed using Omicron Nanotechnology ultra-high vacuum equipment at a pressure below 1.1×10^{-6} Pa. Mg Kα X-ray source was operated at 15 kV and 300 W. Measurements were conducted at room temperature. Analyzes of the obtained results were performed using CASA XPS software package with Shirley background subtraction and least-square Gaussian-Lorentzian − GL (30) curve fitting algorithm. Calibration of the measured spectra to the binding energy of 285 eV for C1s line was conducted.

The electrical conductivity of the STFx dense pellets was measured using the Van der Pauw method [42]. Four silver contacts (electrodes A, B, C, D) were placed on the STFx pellets' surface, forming the square shape. The electrical conductivity (σ) can be obtained with the following equation:

$$\sigma = \frac{ln2}{\pi h} \frac{2}{R_{AB,CD} + R_{CA,DB}} \tag{1}$$

where σ is conductivity of the sample, h is thickness of the sample, $R_{AB,CD(CA,DB)}$ is the resistance, which is determined while applying current to electrodes A(C) and B(A) while the potential is measured between electrodes C(D) and D(B).

The study was performed in the synthetic air (20% O_2) and the temperatures ranging between 200 °C and room temperature with a preheating step at 400 °C for sintering of the contact silver paste. An automatic logging system was used for data collection. The acquired data were used to calculate the activation energy from the formula based on the Arrhenius equation:

$$ln\sigma = \frac{E_a}{k} \times \frac{1}{T} + ln\sigma_o \tag{2}$$

where E_a is an activation energy, σ is an electrical conductivity, T is a temperature, σ_o is a pre-exponential factor, and k is the Boltzmann's constant.

Electrode preparation

Glassy carbon rotating disk electrodes (RDE-GCE, 0.196 cm^2, ALS Co., Ltd) were used as support electrodes for powder catalysts. Before the deposition of the catalyst inks, the RDE-

GCE were polished for 5 min using 0.05 μm polishing alumina solution, sonicated for 10 min in deionized water and isopropanol, respectively, then dried overnight at ambient conditions. The electrocatalyst inks were prepared by mixing 120 mg of the prepared perovskite powders, 120 mg Super P Li Conductive Carbon (Imerys Graphite & Carbon), 11.4 mL Ethyl Alcohol Absolut 99.8% Pure (POCH, Poland), and 1.8 mL of K^+ exchanged Nafion solution.

The Nafion is added as a dispersing and binding agent, however, its strong acidity may cause corrosion of oxide catalysts [43,44]. In order to change the pH of the initial solution (pH of ~1–2) the K^+ exchanged Nafion solution was prepared by mixing 5 wt% Nafion 117 solution (Sigma-Aldrich) with 0.1 M potassium hydroxide solution (1 M KOH Titripur (Merck) diluted with DI water ~12 MΩ) at 2:1 vol ratio, resulting in pH change to ~9.

Subsequently, the prepared inks were ball-milled for 96 h (Zoz Gmbh, Rollermill RM1) in 20 mm diameter glass vial using 1 mm diameter yttria-stabilized zirconia (YSZ) grinding balls with the rotation speed of 100 rpm, followed by sonication in an ice-water bath for 30 min. The milling step was added to crush agglomerates and to better mix the catalyst powder with conductive carbon. SEM observations of inks drop-casted onto Ni foil are presented in Fig. S3. The ink made from the as-prepared powder (by ultrasonic dispersion with Nafion and conductive carbon) has visible agglomerates with diameters of >10 μm. The ink roller milled using 3 mm zirconia balls also ended up with some agglomerates, which were not visible after roll milling using 1 mm balls. Based on these results, all inks were made utilizing roller milling with 1 mm zirconia balls. The level of impurities introduced by milling media is very small, below the detection limit of EDS (<0.5 at.%). The Ni foil was chosen as a support for SEM observations due to the high electrical conductivity and because it does not contain any elements which are constituents of prepared STFx powders. For OER experiments, 5 μL of ink was drop-casted onto the RDE-GCE rotating at 700 rpm, achieving the catalyst mass loading of 45.5 μg. The rotation induced air flow over the casted ink droplet helps to obtain the uniform and homogenous film [45,46].

Electrochemical measurements

All electrochemical measurements were performed in a three-electrode Teflon cell system in 0.1 M KOH aqueous solution (prepared from 1 M KOH Titripur from Merck, diluted with DI water ~12 MΩ). A Hg/HgO in 0.1 M KOH solution (ALS Co., Ltd, Japan), a Pt coil, and a coated RDE-GCE were used as the reference (RE), counter (CE), and working (WE) electrodes, respectively. The electrochemical tests were performed on BP-300 (BioLogic) bipotentiostat connected with a rotating disk electrode (RDE) configuration (RRDE-3A Rotating Ring Disk Electrode Apparatus Ver.2.0, ALS Co., Ltd). An electrolyte temperature of 25 °C was maintained by a Julabo F12 thermostat. Before each experiment, the electrolyte was purged with 99.995% O_2 for 30 min, then the gas flow (50 mL min^{-1}) was kept over the electrolyte in order to maintain the O_2/H_2O equilibrium. The working electrode was activated by potential cycling 10 times in the range of 1.0–1.7 V vs. RHE at a scan rate of 100 mV s^{-1}. Cycling voltammetry (CV) scans were

performed in the non-faradaic potential region of 1.0–1.1 V vs. RHE at scan rates of 10, 20, 40, 60, 80, 100 mV s^{-1} with 0 RPM rotation speed for the double-layer capacitance (C_{dl}) estimation. The electrochemical active surface area (ECSA) was calculated assuming the reference capacitance value of 40 μF cm^{-2} for oxides [47]. CV scans for OER were performed in the range from 1.1 to 1.9 V vs. RHE at a scan rate of 10 mV s^{-1} with 1600 rpm rotation speed. The charge transfer resistance (R_{ct}) was calculated from the electrochemical impedance spectroscopy (EIS) measurements in the frequency range from 10 kHz to 0.1 Hz at 1.7 V vs. RHE with an amplitude of 10 mV and the 1600 rpm rotation speed. Fitting to the modified Randles equivalent circuit was performed with EC-Lab® Software.

All measured potentials were converted to RHE by the experimental calibration of the reference electrode against RHE (Fig. S4) [48]. The value of E_{offset} equals the measured equilibrium potential of hydrogen electrocatalysis (HER/HOR) and was determined to be −928 mV. The potential conversion performed according to the equation:

$$E_{RHE} = E_{measured} + 928 \text{ mV} \qquad (3)$$

For OER polarization curves, the background correction was performed by averaging the positive and negative-going scans [48]. All potential values were iR-corrected to eliminate the solution resistance factor according to the equation:

$$E_{iR-corrected} = E_{applied} - iR_{un} \qquad (4)$$

where i is current and R_{un} is an uncompensated ohmic electrolyte resistance determined by EIS measurement at OCV. The current density was normalized by the geometrical surface area of RDE-GCE (0.196 cm^2) (expressed in the unit mA cm$_{GEO}^{-2}$). The overpotential of OER was calculated using the equation:

$$\eta = E(10 \text{ mA cm}^{-2}) - 1.23 \text{ V } vs \text{ RHE} \qquad (5)$$

The specific activity was determined by current normalization using the BET specific surface area of each oxide catalyst (expressed in the unit μA cm$_{OX}^{-2}$). The catalyst mass activity at specific overpotential was calculated by current normalization by the catalyst mass loading of 45.5 μg (expressed in the unit A g^{-1}). For each material, at least 3 separate samples were prepared and tested, but the typical differences were negligible. The representative OER polarization curves obtained for STF50 are presented in Fig. S5.

Results and discussion

Catalyst structural characterization

$SrTi_{x-1}Fe_xO_{3-\delta}$ (x = 0.35, 0.5, 0.7, 0.9, and 1.0) (STFx) powders were synthesized by the high temperature solid state reaction method. The powders were denoted as STF35, STF50, STF70, STF90, and SFO.

Fig. 1a and b shows the SEM images of the STF70 powder (after the ink milling step). The images of the other powders are presented in Fig. S6. The powders are composed of small particles with diameters <250 nm. For increasing Fe content,

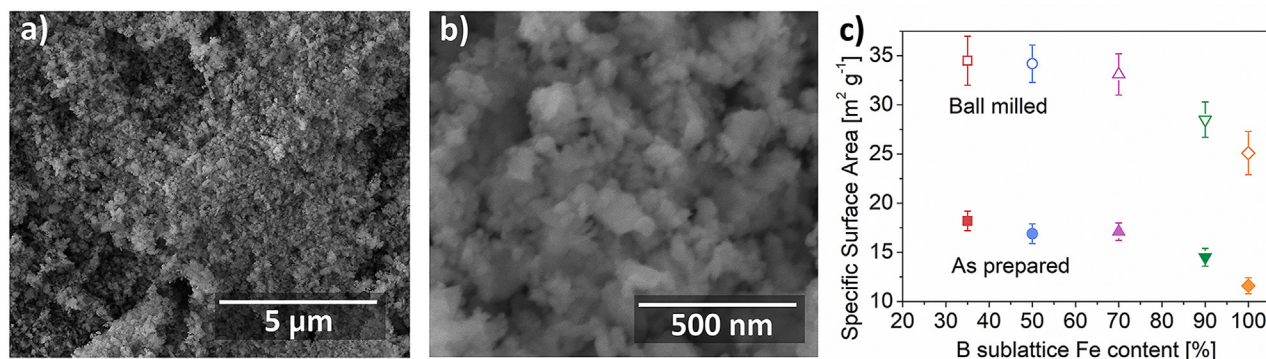**Fig. 1 — SEM images of synthesized STF70 powders (a) low (x10 000) magnification, (b) high (×100 000) magnification, and (c) BET surface areas of the as-produced and ball-milled $SrTi_{x-1}Fe_xO_{3-\delta}$ (STFx) powders.**

the particle size increases. These microscopic observations were confirmed by sorption measurements (see Fig. 1c). As noted, the roller mill procedure reduces the agglomeration, which results in a nearly twofold increase of the specific surface area for ink-milled powders in comparison to the as-prepared. The BET area was the largest for the STF35 powder (~35 $m^2 g^{-1}$), and reduced to ~25 $m^2 g^{-1}$ for the SFO. Even though the SFO powder was prepared at the lowered temperature (1100 °C instead of 1200 °C) it still had a decreased surface area, indicating a stronger sintering/grain growth tendency for the Fe rich sample. Indeed, as investigated by Schulze-Küppers et al. [49], the sintering onset of SFO is ~750 °C and maximum shrinkage occurs at ~1100 °C, whereas for Ti containing compositions, these characteristic temperatures are at least 100 °C higher.

In general, the obtained particle sizes can be considered small, especially with regard to the synthesis route, including high temperature calcination. Such fine morphology should be advantageous for electrocatalysis, where high surface areas lead to high total current densities.

As indicated by Fabbri et al. [50], the surface areas typically obtained for perovskites are <4 $m^2 g^{-1}$, which hinders their practical applications. For example, Su et al. have fabricated powders of $SrCo_{0.9}Ti_{0.1}O_{3-d}$ (SCT), $SrFe_{0.9}TiO_{3-d}$ (SFT) and $Ba_{0.5}Sr_{0.5}Co_{0.8}Fe_{0.2}O_{3-d}$ (BSCF) by a complexing sol-gel method [51]. After the final calcination step at 1000 °C, the obtained BET values were 0.91 $m^2 g^{-1}$, 0.86 $m^2 g^{-1}$, and 0.43 $m^2 g^{-1}$ for SCT, SFT, and BSCF, respectively. Zhu et al. have studied $SrNb_{0.1}Co_{0.7}Fe_{0.2}O_{3-d}$ (SNCF) powders as effective OER catalysts, including the effects of powder ball milling [52]. The as-synthesized powder had a surface area of 0.25 $m^2 g^{-1}$, whereas after milling the area increased to 6.45 $m^2 g^{-1}$. The raw powder seems to have been highly agglomerated. Cheng et al. have studied BSCF catalysts in the form of the as-produced and ball-milled powders. The surface area increased upon milling from 3 $m^2 g^{-1}$ to 5 $m^2 g^{-1}$ [53]. In the case of $SmBa_{0.5}Sr_{0.5}Co_2O_{6-d}$ (SBSC) fibers prepared by

electrospinning [54], the BET surface area varied from ~13 $m^2 g^{-1}$ for fibers calcined at 800 °C down to 3 $m^2 g^{-1}$ after calcination at 1100 °C. For the synthesis of dedicated high surface area perovskites, Fabbri et al. used a flame spray synthesis, which produced BSCF and LSC powders with high specific surface areas of ~25 $m^2 g^{-1}$ and ~46 $m^2 g^{-1}$. In contrast, traditionally prepared BSCF and LSC powders were characterized by specific surface areas of 4 and 1.5 $m^2 g^{-1}$.

Interestingly, our results show that it is possible to obtain high surface area (>30 $m^2 g^{-1}$) perovskite powders even using traditional high temperature synthesis methods. This opens the possibilities to produce technically relevant powders via traditional powder processing routes.

Fig. 2a shows the powder XRD patterns of the prepared STFx perovskites. All of the prepared samples crystalized in a cubic crystal structure (space group *Pm-3m*, No. 221). The position of the characteristic reflection (110) shifted towards higher 2θ angles with increasing Fe content in the perovskite structure, indicating the reduction of a lattice size (exact values are presented in Table S1). Fig. 2c shows the lattice parameters obtained from the Le-Bail refinement as the function of Fe content (refinement plots are demonstrated in Fig. S7).

The plot also includes the available unit cell data that is found in the literature for the end-members: $SrTiO_3$ (COD ID 7212245) and $SrFeO_{2.96}$ (COD ID 1528364), the line (Vegard's slope), which follows the composition $Sr(Ti^{4+})_{1-x}$ $(Fe^{4+})_xO_3$ [41,55]. The +4 valence state of iron (ionic radii 0.585 Å) would mean full iron oxidation, which is rarely the case at the standard conditions [44]. The oxidation state of iron equal to 3+ was reported for STFx compounds sintered in nitrogen, while it reduced the iron ions. As proposed by Rothschild et al. [33] the proper framework to analyze the STFx materials family is the $Sr^{2+}(Ti^{4+}_{1-x}Fe^{3+}_x)O_{3-x/2-d}$, though the STFx typically also contains a considerable amount of Fe^{4+}, which is a charge carrier (hole) and is believed to be an important factor in creating an optimal O–Fe covalency for OER [21]. The Fe^{3+} in
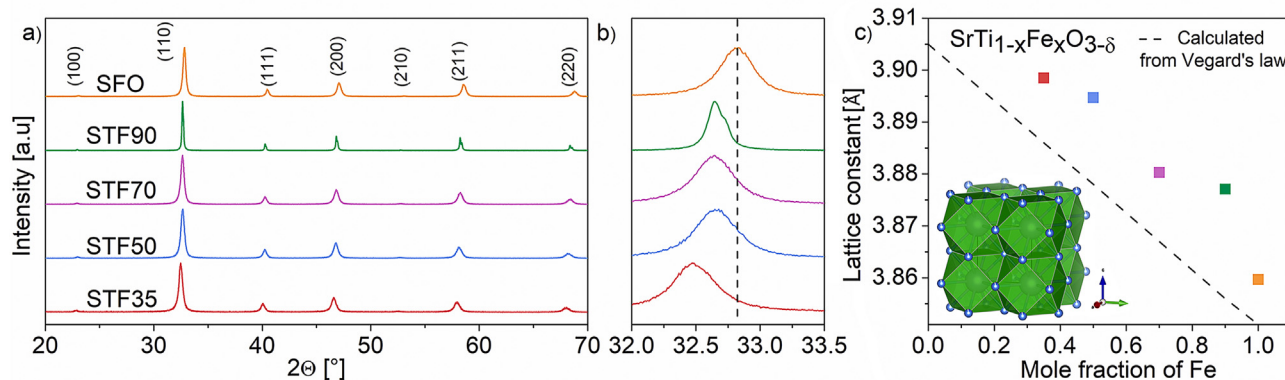
Fig. 2 – (a) Powder XRD patterns of synthesized $SrTi_{x-1}Fe_xO_{3-\delta}$ (STFx), (b) zoom-in of the patterns showing the main reflection (110) shift, (c) and calculated unit cell parameters.

the high spin state has a relatively large diameter (0.645 Å), which should result in an expansion of the unit cell upon substitution of Ti^{4+}, which is not experimentally observed. One of the possibilities is a formation of a low spin (LS) Fe^{3+} (0.55 Å), which would result in unit cell size reduction. The issue has been discussed for a similar material system of $SrSn_{1-x}Fe_xO_{3-d}$ [56].

Filatova et al. have used soft X-ray XAS to determine the atomic and electronic structure of STFx powders [57]. The analysis of Fe2p ($L_{2,3}$) absorption spectra revealed the main state of Fe to be +3 with part of iron ions at +4 state. The authors confirmed the octahedral position of the Fe cations in perovskites. Interestingly, for higher Fe content samples, there is also a possibility of Fe^{3+} at tetrahedral positions and even for some Fe^{2+} at octahedral position.

Formation of the oxygen vacancies (and more generally, changes in oxygen stoichiometry), resulting from the charge compensation of Fe^{3+} substitution, might also result in unit cell size changes. STFx compounds are also sometimes considered as "oxygen deficient" perovskites [58], where oxygen content is decreased, but no vacancies are formed. The oxygen vacancies are reported to have a similar (+- 10%) size as oxygen ions in the lattice [59], so they typically have a smaller influence on the unit cell size than the cation changes. The change in oxygen content might result in the formation of $O–Fe–O$ or $O–V_o^{·}–O$ complexes, which have been reported to change the coordination number of Fe from 6 to 5 and thus change the ionic radii of iron.

It has also been reported, that in the case of STFx materials, the XRD does not fully resolve the crystallographic structure [60,61]. Steinsvik et at. employed advanced electron microscopy (selected area diffraction – SAD and electron energy loss spectroscopy - EELS) for characterization of STFx materials [61]. The authors reported formation of the superstructures due to oxygen vacancies ordering in iron rich STFx.

All of these effects can have a complex influence on the unit cell size where basic predictions based on Shannon's ionic radii principles are not precise.

Though the STFx seem to present a complex cationic structure, some of the reported crystallographic data is fairly consistent. The unit cell dimensions obtained in the present work agree very well with several of the reported literature values. Schulze-Küppers et al. reported the lattice parameter of ~3.905 Å and ~3.895 Å for the 0% and 50% Fe containing compositions, respectively [49]. The lattice constant was also consistently higher than theoretically expected based on Fe^{4+}. Miruszewski et al. studied the full range of STFx compositions and obtained ~3.895 Å for the 50% iron composition and ~3.860 Å for the 100% iron composition, the same as in the current work [62].

Based on the obtained data and the available literature, it might be concluded that the composition of the perovskites synthesized in this work contains a mixture of octahedrally coordinated Fe^{4+} and Fe^{3+}.

Further microstructural characterization of STF70 powder was performed by transmission electron microscopy (TEM). In Fig. 3a–c the high-angle annular dark-field (HAADF) and bright field (BF) images are presented. The observed area consists of an agglomerate of nanocrystals up to 200 nm in size, which is consistent with SEM imaging of the powders. The selected area electron diffraction (SAD) patterns (Fig. 3d and e) indicate the well-defined polycrystalline cubic structure of the Pm-3m space group, which agrees with the macroscopic XRD results. Uniform dispersion of the constituent elements (Sr, Fe, Ti) was confirmed by TEM-EDS elemental analysis (Fig. 3f–j). As observed in TEM images, the STF70 particles can be considered relatively small even though the powder was obtained via sintering at 1200 °C, which usually leads to a formation of the micrometric particles.

The full XPS element survey scans of $SrTi_{x-1}Fe_xO_{3-\delta}$ powders are presented in Fig. S8. Peaks corresponding to Sr, Ti, Fe, O and C are clearly observed (the detected carbon is associated with the species adsorbed from the ambient air). The performed XPS spectra fitting is demonstrated in Fig. 4. The Sr3d spin-orbit doublet has been deconvoluted into pairs originating from different Sr chemical coordination, i.e. perovskite lattice Sr at lower binding energies along with secondary phases at higher binding energies, all with an energy separation of 1.8 eV. The distinguished secondary phases (most likely $SrCO_3$) result from
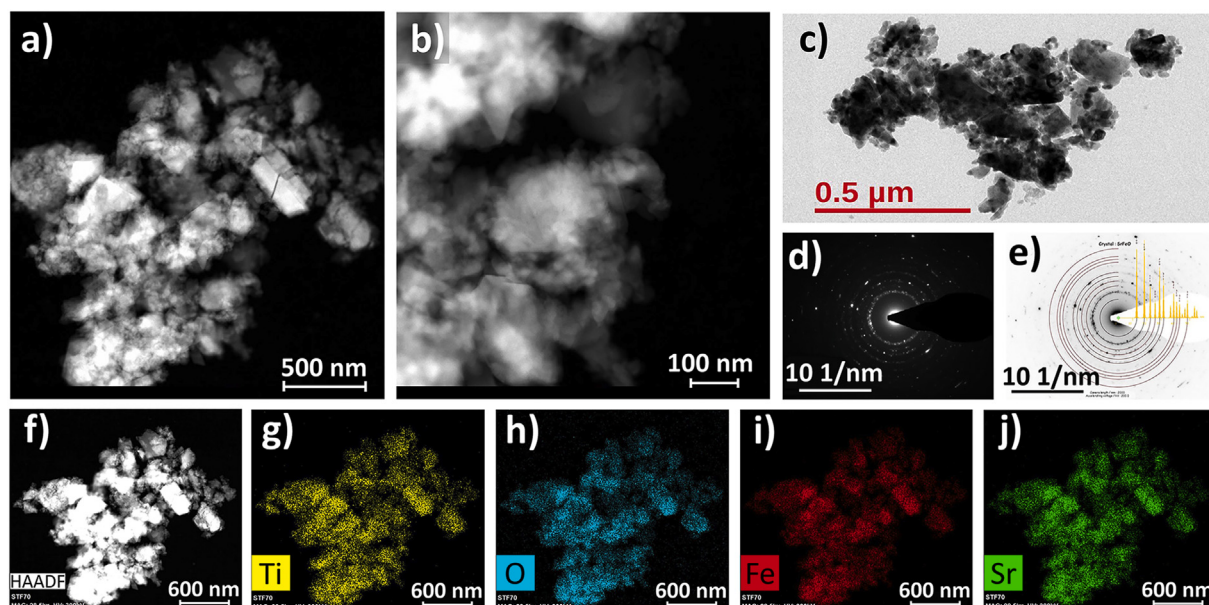
Fig. 3 — (a–c) HAADF-(S)TEM images and (d) corresponding SAD pattern with (e) superimposed theoretical pattern of the STF70. (f–j) TEM-EDS elemental maps of (g) titanium, (h) oxygen, (i) iron, (j) and strontium.

the Sr surface segregation and are the products of Sr reaction with chemisorbed gases [63–65]. Two kinds of Fe species were detected in the Fe2p spectra, Fe^{3+} and Fe^{4+} with an energy separation of 13.6 eV. It points out that the perovskite structures examined in this work should be described as $SrTi_{1-x}[Fe^{3+}, Fe^{4+}]_xO_{3-\delta}$, consistent with the discussion in the XRD results section. For comparison, Ghaffari et al. synthesized $SrTi_{x-1}Fe_xO_{3-\delta}$ (x = 0, 0.2, 0.4, 0.6, 0.8 and 1) powders via HT-SSR technique and observed a systematic decrease of Fe^{3+}/Fe^{4+}

ratio from 2.83 for x = 0.2 to 1.28 for x = 1 [66]. Interestingly, in our study, the Fe^{3+}/Fe^{4+} ratio was relatively constant with a value ~1.5. The relative amount of Sr and Fe species calculated from the areas of deconvoluted peaks is collected in Table S3 and Table S4.

Measured O1s spectra in Fig. 4c presents the changes of the surface oxygen species of STFx powders with higher Fe content in B sublattice. The lowest observed binding energy of O1s for STF50 and STF90 was ~526 eV, when in fact the lowest
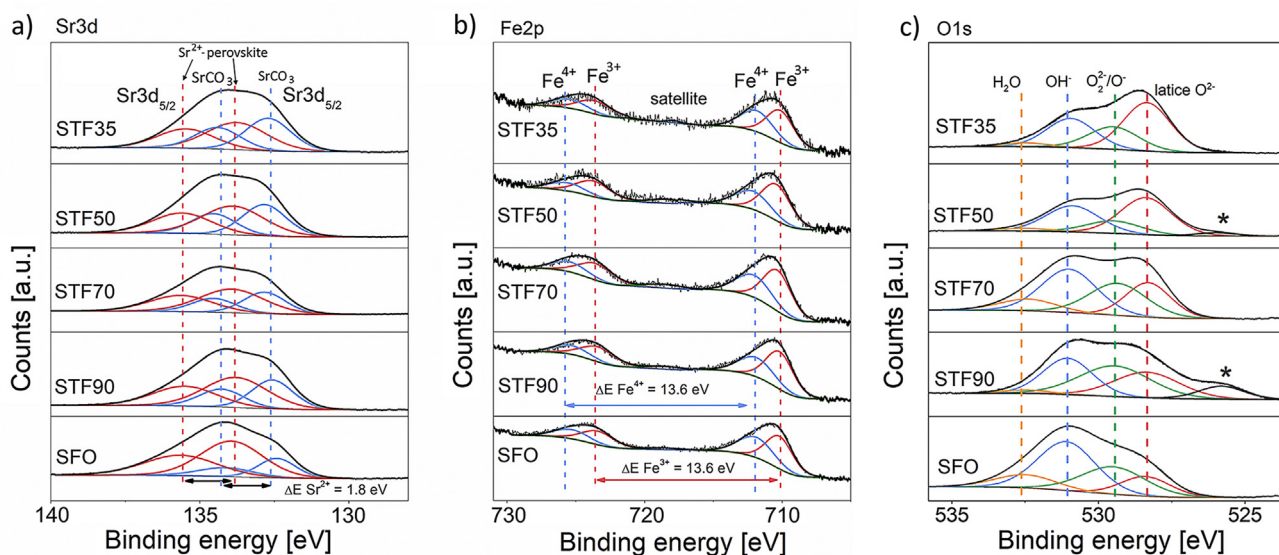

Fig. 4 — (a) Sr3d, (b) Fe2p and (c) O1s X-ray photoelectron spectra of $SrTi_{x-1}Fe_xO_{3-\delta}$ powders.
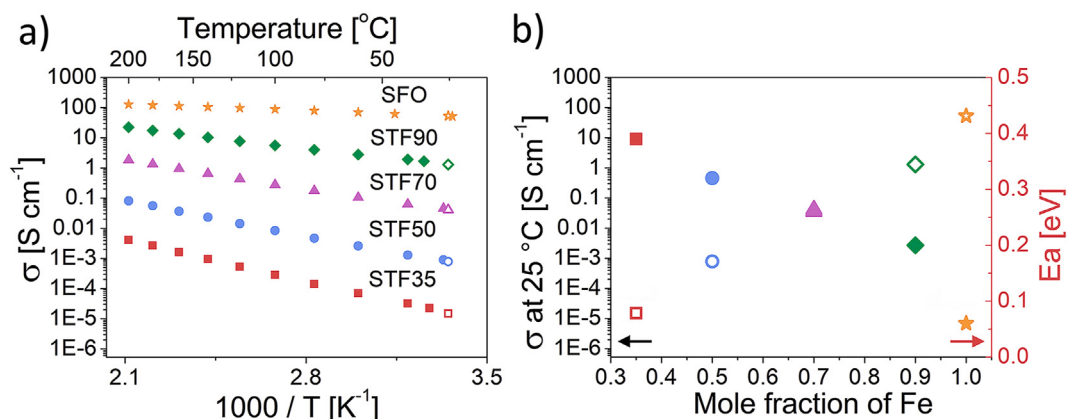
Fig. 5 — (a) Temperature dependence of SrTi$_{x-1}$Fe$_x$O$_{3-\delta}$ (STFx) measured DC electrical conductivity (filled symbols) and extrapolated value of conductivity at 25 °C (blank symbols). (b) Activation energies of electrical conductivity (filled symbols) and the extrapolated electrical conductivity at 25 °C (blank symbols) as the function of Fe mole fraction in SrTi$_{x-1}$Fe$_x$O$_{3-\delta}$ perovskite structure.

expected one is 528 eV for metal oxides. Those additional artifact signals (marked by *), may be due to the "double charge" effect and/or hardware issues [67]. It is likely that the signal from the carbon tape (to which the powders were glued) was also collected during the analysis. However, the shape changes of the spectra with Ti substitution by Fe may be assigned to the increase of highly oxidative oxygen species (O_2^{2-}/O^- at ~528.3 eV) concentration associated with the surface oxygen vacancies (the calculated values are gathered in Table S5) [68]. The XPS spectra of Ti2p indicates that Ti was in +4 oxidation state (Fig. S9).

Electrical conductivity study

The DC electrical conductivity of SrTi$_{x-1}$Fe$_x$O$_{3-\delta}$ (STFx) materials was measured on sintered pellets by Van der Pauw method in the temperature range from 200 °C to ambient in air.

The results are presented in Fig. 5a and summarized in Table S2. The conductivity values increase considerably with the increasing Fe content [36] and represent a thermally activated process. The six orders of magnitude increase from ~10^{-5} S cm^{-1} to ~50 S cm^{-1} between the STF35 and SFO samples at 25 °C is consistent with literature reports [29,69]. As evidenced in Fig. 5b, the increase of conductivity seems to follow a logarithmic dependence on the Fe content. The calculated activation energies of the electrical conductivity, presented in Fig. 5b, decrease linearly with the higher mole fraction of Fe and are in the range from 0.39 eV to 0.06 eV.

The defect chemistry of STFx has been considered in detail by Rothschild et al. [32] and Kuhn et al. [70]. The energy band diagram for STFx has been proposed by Rothschild. With increasing Fe concentration, the valence band was proposed to shift closer to the conduction band. The band-gap energy varies from 3.2 eV for STO to ~2 eV for SFO. The top of the valence band formed by Fe^{3+}/Fe^{4+} redox pairs is overlapping with the top of the O2p band, similarly as is the case of

strontium ferrite [32]. In the oxidizing conditions used in this work, as discussed by Perry et al. the predominant electronic species (in the case of STF35) are holes [71]. Assuming localization of holes on iron (redox active ion), the concentration of the holes is proportional to [Fe^{4+}] with the Fe^{3+} being the neutral species. As discussed in the XPS section, the relative ratio of Fe^{3+}/Fe^{4+} seems to be constant for different STFx compounds, but the overall charge carrier concentration increases with the increasing Fe content in STFx. The increasing Fe^{3+}/Fe^{4+} charge carrier (localized holes) concentration explains the increasing conductivity values and translates into lowered activation energy.

Such a high difference of the electronic conductivity obtained for the different STFx materials is an interesting case for the comparison with the electrocatalytic measurements. The increased electronic conductivity is usually correlated with an improvement of the overall charge transport and hence boosts the electrochemical performance of the catalyst [72,73]. STFx in general, represent lower values of room temperature conductivity than some of the most active perovskites, e.g. the conductivity of La$_{0.6}$Sr$_{0.4}$CoO$_{3-\delta}$ (LSC64) exceeds 600 S cm^{-1} [74] and the conductivity of (La,Sr)FeO$_{3-\delta}$ is within 1−10 S cm^{-1} range [75].

Cheng et al. have studied ex-situ (based on compressed powders) electronic conductivity of the La$_{1-x}$Sr$_x$CoO$_3$ (x from 0 to 1) [76]. The A-site cation was varied between a larger Sr^{2+} (1.44 Å) and smaller La^{3+} (1.36 Å), whereas the B-site, redox active cation remained unchanged. The authors also reported a wide range of electrical conductivity values, ranging between ~$3\cdot10^{-5}$ S cm^{-1} for LaCoO$_3$ to 0.3 S cm^{-1} for La$_{0.2}$Sr$_{0.8}$CoO$_3$. In their case, the crystallographic structure of the materials varied across different x (Sr) levels, so there was a difference in both crystal structure and its electrical conductivity. In the case of STFx, the cubic structure was retained, which makes the influence of the electronic conductivity of the STFx materials more directly comparable. The work by Cheng et al. also shows the possibility to tailor the
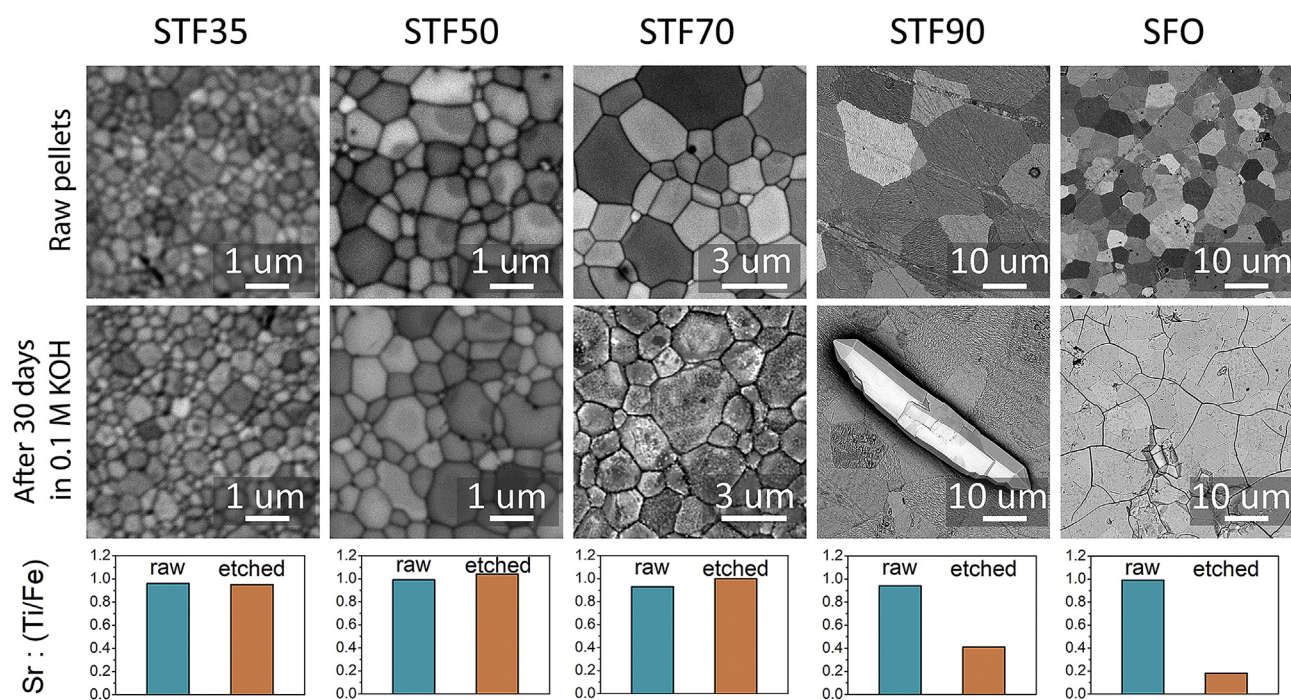
Fig. 6 – $SrTi_{x-1}Fe_xO_{3-\delta}$ pellets chemical stability test performed in 0.1 M KOH.

conductivity value of STF by modification of the A-site cations by partial substitution by La, which might be an interesting topic for future studies.

Conductivity within the STFx system was studied by Hayden et al. based on the 300 nm thin-film samples prepared by physical vapor deposition [34]. The electrical conductivity values were ranging from 10^{-5} S cm^{-1} for STF50 to 0.043 S cm^{-1} for pure SFO. Above a Fe content of 0.75, the conductivity plot remained constant. The values reported in our work differ by even two orders of magnitude in comparison to results obtained by Hayden. The lower than expected conductivity values were attributed by the authors to the potential oxygen deficiency of the films.

Chemical stability of the catalysts

The stability of the strontium-based perovskite compounds at high pH solutions has not been studied in sufficient detail. Several works have emphasized the dissolution of strontium in alkaline solutions [65,77]. However, the influence of the B-site cations on the solubility of the A-site strontium has not been discussed thoroughly.

For the purpose of the present work, the chemical stability of $SrTi_{x-1}Fe_xO_{3-\delta}$ (STFx) was studied using a 30-day immersion test of sintered pellets in an alkaline solution (0.1 M KOH, pH~13). The materials were thus studied without external electrochemical polarization, i.e. purely chemical degradation has been examined. The pellets were prepared in the same manner as the pellets for the electrical conductivity test. To evaluate the extent of Sr dissolution, the surfaces were analyzed for the chemical composition changes via electron microscopy and EDS spectrometry. The results are presented in Fig. 6. The images in the first row of Fig. 6 present surfaces of the sintered pellets after mechanical polishing and thermal etching, which can be considered the initial state, prior to exposure in alkaline solution. The images in the second row of Fig. 6 show the surfaces of the pellets after a 30-day-long exposure to 0.1 M KOH solution. The samples with low Fe content (STF35 and STF50) did not show visible morphological changes. The samples with increased iron content showed increased altering of the surface morphology. The surface of STF70 exhibited an observable increase of roughness, but the individual grains and grain boundaries were still observable. On the STF90 pellet surface, the growth of Sr-rich crystals was noticed (further analyzed by EDS in Fig. S10, the new phase is most likely $SrCO_3$). The grain morphology was still visible, but the grain boundaries, promoted initially by thermal etching, were chemically etched and thus less visible. The surface of SFO shows prominent changes, where no grain/grain boundaries could be observed. The surface also shows large cracks/trenches caused by the etching of Sr.

The morphological changes are connected to the dissolution of Sr from the surface. The EDS results of the studied surfaces are shown in the third row of Fig. 6. The graphs show a ratio of A-site and B-site cations in the perovskite structure (all EDS data is gathered in Table S6). It evidences the
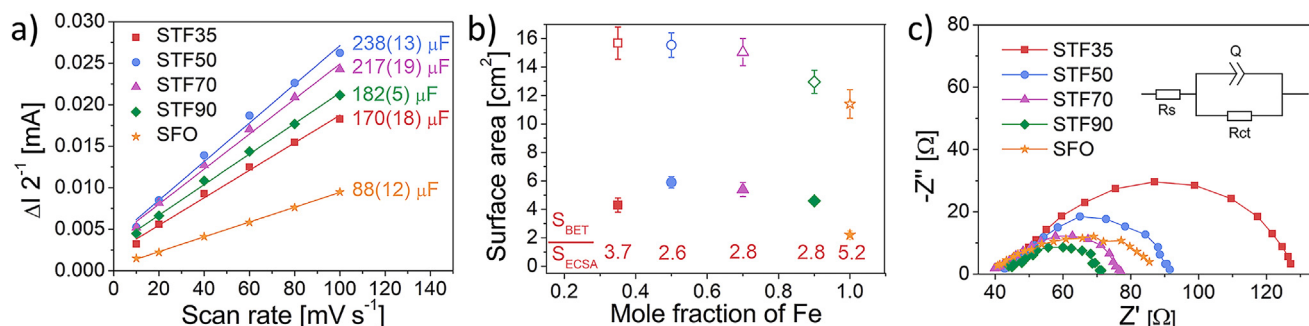
Fig. 7 – (a) Double layer capacitance, (b) comparison of catalyst BET SSA (open symbols) and ECSA (filled symbols) (c) EIS spectra at potential of 1.7 V vs. RHE. Electrochemical tests were performed in 0.1 M KOH electrolyte.

substantial Sr loss in the surface layer of STF90 and SFO pellets due to the chemical degradation. STF70 shows no Sr dissolution, but the pellet surface is rougher after the immersion test, which might indicate the onset of the reaction. The STF50 seems to be unchanged by alkaline environment; no elemental and morphological changes were observed. This observation was further confirmed by cross section studies of STF50 pellets before and after a 30-day-long exposure to 0.1 M KOH solution presented in Fig. S11.

The additional test in Ar-bubbled KOH solution proved that the large crystals visible on STF90 surface are due to a reaction with CO_2 dissolved in electrolyte. Although its amount is very small, it readily reacted with Sr forming $SrCO_3$. The removal of CO_2 from the electrolyte had no visible influence on Sr leaching, which was still pronounced (Fig. S12).

Dissolution of Sr in STFx has also been highlighted by Hayden et al. [34] in their thin film study. They analyzed the chemical content of the films (by EDS) before and after the electrochemical cycling (oxygen evolution reaction). The authors explained the dissolution of Sr in iron-rich compounds by an electrochemical process involving redox active $Fe^{3+/4+}$. Based on our results, the degradation can be narrowed down to a chemical dissolution, not necessarily occurring under oxygen evolution potentials (>1.23 V vs. RHE) but also, to a large extent, at open circuit potential (1.1 V vs. RHE).

The pellet-exposure test showed an important influence of Ti^{4+} content on chemical stability. The compositions with relative Fe content not exceeding 50% seem to be stable chemically, which is an important determinant for materials application.

Electrocatalytic activity

The electrocatalytic activity toward the OER of the $SrTi_{x-1}Fe_xO_{3-\delta}$ (STFx) perovskites was evaluated in 0.1 M KOH solution (pH ~13). Firstly, the electrochemically active surface area (ECSA) was determined. Fig. 7a illustrates the relationship between the current density and the scan rate obtained from cyclic voltammetry in the non-faradaic potential region (at 0 rpm). The values of ECSA estimated from the measured C_{dl} are presented in Fig. 7b. ECSA is a commonly implemented descriptor of metal oxide active sites, accessible for electrocatalysis reactions [48,78–82].

To facilitate the comparison, BET SSA values of the ball-milled catalyst presented in Fig. 1 were multiplied by the mass of the drop-casted catalyst.

For STF35, a low value of ECSA was found. The reason might be the low amount of redox active Fe in the B-site, dominated by the Ti^{4+}. For low Fe content, the percolation between the Fe-containing octahedra cannot form, possibly
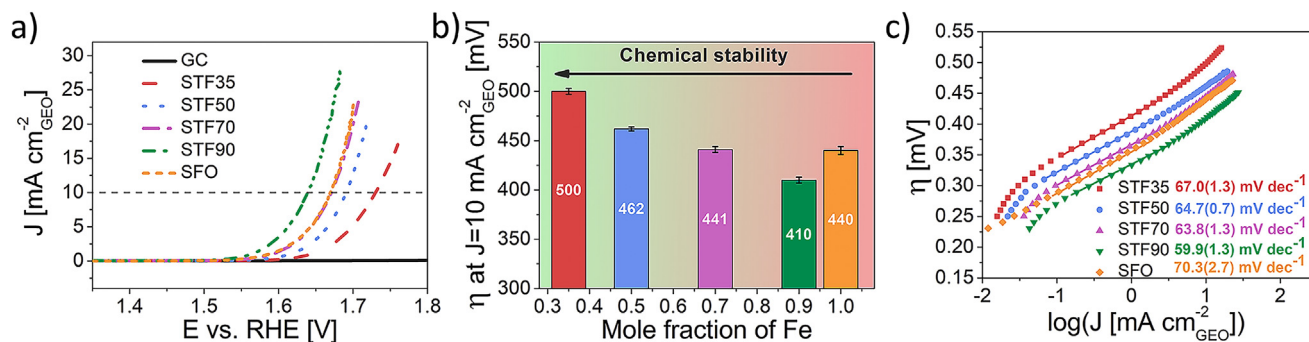

Fig. 8 – (a) OER polarization curves, (b) the overpotentials (η) at 10 mA cm^{-2} current density, and (c) and corresponding Tafel plots measured in O_2 saturated 0.1 M KOH at 10 mV s^{-1} with the rotation speed of 1600 rpm.
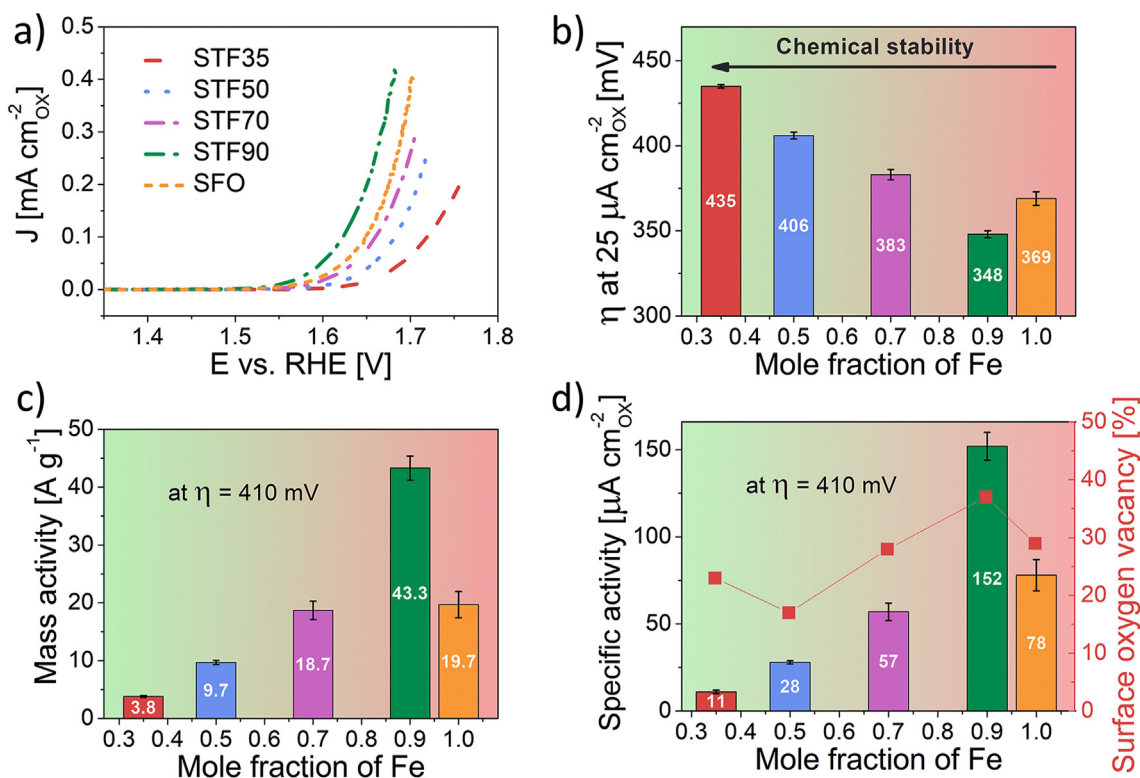
Fig. 9 − (a) OER polarization curves with current density normalized by BET SA, (b) specific surface activity, (c) mass activity and (d) relationship between specific activities and surface oxygen vacancies of $SrTi_{x-1}Fe_xO_{3-\delta}$ (STFx) catalyst powders.

influencing the electrocatalytic activity. The highest ECSA was obtained for the STF50, which also showed the highest BET specific surface area. For the STF70 and STF90, the ECSA showed a decrease. The most likely reason for this was the lower BET specific surface area of these powders. Interestingly, the ratio of BET SSA to ECSA was the same for STF50, STF70, and STF90. Increasing the relative iron content in STFx had no visible influence on the active sites, at least when taking into account ECSA. Pure SFO showed relatively low ECSA with a significant divergence between the ECSA and BET surface areas, possibly caused by the chemical instability of the material.

The electrochemical impedance spectroscopy (EIS) was used to determine the charge transfer resistance (R_{ct}) of the catalysts, one of the factors determining the enhanced activity toward OER [83−85]. The Nyquist plots of all prepared materials are illustrated in Fig. 7c. The incorporation of iron into the perovskite structure induced a systematic drop of the R_{ct} from 90 Ω for STF35 to 28 Ω for STF90 (Table S7). The SFO sample, without structure stabilizing titanium ions, again does not fit the measured trend.

The general OER performance of the $SrTi_{x-1}Fe_xO_{3-\delta}$ (STFx) perovskite catalysts, determined based on the geometrical surface area of the glassy carbon (GC) electrode, is presented in Fig. 8a. The performance of a blank glassy carbon electrode

is shown for comparison. The pure SFO shows high performance, inferior only to STF90, but again, SFO does not follow the trend for Ti and Fe-containing samples. The influence of Sr dissolution cannot be accounted for, so it is hard to accurately compare the SFO with Ti/Fe-containing compounds. For the latter, the overall activity toward OER increases monotonically with increasing Fe content in the perovskite structure. As the first benchmark, the overpotentials (η) at 10 mA cm^{-2} current density (based on the geometric area of GC) are presented in Fig. 8b. For the stable STF35 and STF50 perovskites, the overpotentials of 500 mV and 462 mV were obtained. For the less stable STF70 and STF90, lower overpotentials of 441 mV and 410 mV were achieved, with the latter being the lowest. SFO showed an overpotential of 440 mV at 10 mA cm^{-2}. The relative errors, as obtained for three different electrodes, were small, indicating good reproducibility of the measurements, also taking into account the relative instability of the Fe-rich materials. For comparison, the pure RDE-GC electrode demonstrated unnoticeable activity what evidences the negligible contribution into current density growth during OER experiments.

Analysis of the Tafel plots, illustrated in Fig. 8c, revealed that all examined materials are driven by the similar OER mechanism (comparable values of Tafel slopes, 60−70 mV dec^{-1}). The slope of ~60 mV dec^{-1} for STF90 indicates the

chemical step to be the rate-determining step of OER [86]. The higher values of Tafel slopes obtained for the rest of the examined perovskite materials suggest a possibility of a mixed mechanism (e.g. a parallel process) to have an impact on overall OER performance. The Tafel slope of the SFO material was ~70 mV dec^{-1}, which again indicates different behavior of this compound.

Based on the measured BET specific surface areas of the catalysts, the surface specific performance metrics can be compared. The OER polarization plots with the current density normalized by BET specific surface area are presented in Fig. 9a. As the surface of the catalysts was comparable, the trend of surface-specific catalyst activity remained unchanged. Fig. 9b depicts the overpotential determined at 25 μA cm^{-2} (in respect to oxide surface area). The lowest overpotential value of 348 mV was obtained by STF90, followed by 369 mV for SFO. For the stable STF50, an overpotential of 406 mV was determined. Another useful performance metric is the mass specific benchmark, though there is no standard overpotential value for which it is reported. Fig. 9c presents the mass activities of the catalysts determined at the arbitrary overpotential of 410 mV (value of STF90 to achieve a geometrical current density of 10 mA cm^{-2}). The mass activity of the stable STF50 is ~10 A g^{-1}, whereas for the unstable STF90 it is 4x higher. Fig. 9d correlates the specific activity with relative surface oxygen vacancy concentration estimated by XPS studies. The increasing OER performance of STFx with oxygen vacancies is observed. However, due to the pronounced instability, the SFO does not follow the trend.

It has been considered that oxygen vacancies in perovskites can improve the electrocatalytic performance toward OER. For instance, Lu et al. have created oxygen vacancies in LaCoO$_3$ perovskite by Sr doping and Ar plasma treatment [87]. It was shown that abundant oxygen vacancies acted as active sites and showed high intrinsic activity. Oxygen vacancies concentration increase, promoted by partial Sr^{2+} substitution for La^{3+}, resulted in Tafel slope decrease from 92.1 to 74.2 mV dec^{-1} for LaCoO$_{3-\delta}$ and La$_{0.7}$Sr$_{0.3}$Co$_{3-\delta}$, respectively. Additionally, the Ar plasma treatment was applied to further manufacture oxygen vacancies and the Tafel slope reduction of La$_{0.7}$Sr$_{0.3}$Co$_{3-\delta}$ to 70.8 mV dec^{-1} was reported. Hona and Ramezanipour reported the facile synthesis method of the oxygen-deficient SrMnO$_{3-\delta}$ [88]. It was shown that the electrocatalytic properties are correlated with the structure and oxygen vacancy. SrMnO$_{2.5}$, the most oxygen-deficient among prepared materials, exhibited the best electrocatalytic activity for the OER. She et al. have established a direct correlation between the surface oxygen vacancies along with the surface Fe oxidation state and the specific activity enhancement of the La$_{1-x}$Sr$_x$FeO$_{3-\delta}$ (x = 0, 0.2, 0.5, 0.8 and 1) [89]. In their work, they found the optimum amount of surface oxygen vacancies in La$_{0.2}$Sr$_{0.8}$FeO$_{3-\delta}$, resulting in the lowest OER overpotential and Tafel slope among examined catalysts.

The activity of the STFx (given by specific overpotential values) seems to correlate linearly with the amount of iron in the perovskite, especially for the compounds with Ti. The cubic perovskite structure is retained for all the studied compounds. Moreover, the (logarithm) of the total electrical conductivity increases linearly vs. the iron content. For the compound without Ti, the electrochemical activity, which is

inferior to STF90, might be decreased due to the rapid dissolution of Sr, also influencing the Tafel slope of the catalyst. The two other high-Fe content compounds (STF90 and STF70), although show high electrochemical performance, also tend to dissolve Sr, rendering them not stable. Hayden et al. have proposed that the reason for the increased Sr-dissolution at high Fe-compounds, might be the activation of the lattice oxygen mechanism (LOM) [34]. Our study has shown that the dissolution occurs also at OCV, where no oxygen evolution takes place, so the origin is purely chemical. The Tafel slope obtained for all the STFx materials was quite similar. In the case of triggering LOM mechanism, a change in Tafel slope could probably be expected [90]. Though the mechanism and the relative scale of A-site Sr-dissolution of OER catalysts are not clear, our work shows that the presence of Ti ions (up to 50/50 Fe/Ti composition) stabilize the perovskite structure and limits the A-site cation dissolution. The Tafel slope of ~60 mV dec^{-1}, obtained for all STFx compounds can arise from the rate limiting reaction: MOOH + OH$^-$ <=> MOO$^-$ + H$_2$O [91]. The Tafel slope of ~60 mV dec^{-1} is often reported for high performance perovskites [92]. In this case, increasing the number of active sites (able to create MOO$^-$/MOOH - Fe in B-site octahedra) would lead to increasing electrochemical performance, which is consistent with our work. On the other hand, the proposed rate limiting mechanism does not involve the electronic charge carriers. Therefore, the observed dependency of the performance vs. electrical conductivity is a secondary, non-critical aspect. It is affirmed by the fact that for the less conducting, lower Fe-content compounds, a slight increase in the Tafel slope has been observed. The electronic conductivity is nonetheless the requirement for efficient charge collection, thus its value should be maximized for efficient electrode materials. Based on these assumptions, we propose that in the case of STFx materials, the active sites include metal ion site (adsorbate evolution mechanism).

The recently reported OER results for perovskites are collected in Table S8. The presented data defines STFx as decent OER catalysts. Due to presented stability issues, only the STF50 shows a reasonable mixture of stability and performance. It shows an overpotential of 460 mV at 10 mA cm^{-2}, which might seem quite high, but taking into account its high surface area (~35 m^2 g^{-1}), the oxide surface (406 mV at 25 μA cm^{-2}) and mass specific (~10 A g^{-1} at 410 mV) performance, it is comparable to other perovskite catalysts.

In the study by Hayden et al. [34] on thin films, the analysis of the onset (ignition) potential and current density achieved at 370 mV (1.6 V vs. RHE) showed improved performance of Fe-rich compositions. The authors concluded that high OER activity was correlated with the low stability of the oxides. For high Fe catalysts, participation of lattice oxygen in OER was discussed. The composition based on 50Fe/50Ti has been proposed as a viable, stable catalyst, which showed the current density at 370 mV of ~2 mA cm^{-2}, comparable to the performance of STF reported here (taking into account the geometric area).

The best perovskite OER catalyst is the monoclinic SrIrO$_3$ developed by Yu et al. [93]. The noble metal containing catalyst was prepared by solid-state reaction, which resulted in powder with BET of 14.6 m^2 g^{-1}. In 0.1 M KOH, the overpotential required for 10 mA cm^{-2} (geometric area) was

~300 mV with a low Tafel slope of 42 mV dec^{-1} and the mass activity of ~50 A g^{-1} (at 320 mV).

$SrCo_{0.9}Ti_{0.1}O_{3-d}$, $SrF_{0.9}Ti_{0.1}O_{3-d}$ and $Ba_{0.5}Sr_{0.5}Co_{0.8}Fe_{0.2}O_{3-d}$ perovskites (with surface areas of <1 m^2 g^{-1}) were studied by Su et al. [51] In 0.1 M KOH, the materials showed overpotentials of 510 mV, 520 mV and 490 mV, much higher than in the present study. The respective Tafel slopes were 88 mV dec^{-1}, 102 mV dec^{-1} and 84 mV dec^{-1}, indicating inferior kinetics than in our case.

Zhu et al. proposed $SrNb_{0.1}Co_{0.7}Fe_{0.2}O_{3-d}$ (SNCF) as a highly active catalyst for OER [52]. Similarly to STFx, SNCF contains a single A-site cation (Sr) and the B-sublattice contains Fe. The material was prepared by solid state reaction and benchmarked against BSCF. The low surface area (<1 m^2 g^{-1}) SNCF showed an overpotential (in 0.1 M KOH, at 10 mA cm^{-2}) of 500 mV, which decreased to 420 mV for ball milled (BM-SNCF) powder (surface area ~6 m^2 g^{-1}). The BSCF showed an overpotential of 510 mV. The Tafel slopes for the SNCF and BM-SNCF were 76 mV dec^{-1} and 90 mV dec^{-1}, respectively. Even though the overpotential obtained for BM-SNCF was lower than for un-milled SNCF, the specific activity was not improved by the milling. The mass activity of the BM-SNCF was ~93 A g^{-1} (at 500 mV).

In comparison to many good oxide catalysts developed in the last years, STF50 is based on abundant, environmentally friendly elements and shows a comparable performance, which can make it an attractive alternative as the OER catalyst.

Conclusions

The series of $SrTi_{1-x}Fe_xO_{3-\delta}$ with x = 0.35, 0.50, 0.70, 0.90 and 1.00 (STFx) perovskites have been fabricated via the solid state reaction synthesis technique and tested as potential oxygen evolution catalysts in alkaline electrolyte. The powders showed a remarkably high specific surface area of >30 m^2 g^{-1}. The chemical stability test, based on immersion of pellets in the electrolyte, indicated that up to Fe content of 50%, the materials were stable in 0.1 M KOH, whereas the samples with higher Fe content showed dissolution of strontium. The surface morphology change induced by Sr dissolution was especially pronounced for the $SrFeO_{3-\delta}$ (SFO) composition. Electrocatalytic oxygen evolution tests showed an inverse linear correlation (excluding the unstable $SrFeO_{3-\delta}$) between the iron content and OER overpotential. Overall, the samples presented satisfactory performance, especially when surface specific values were compared. The redox active B-site containing $Fe^{3+/4+}$ together with inherent surface oxygen vacancies and the high surface area of the catalyst powders provide performance which is comparable to other recently reported highly active perovskite catalysts. Based on earth abundant and non-toxic elements, the $Sr(Ti,Fe)O_{3-\delta}$ (STFx) materials are an interesting, environmentally friendly catalyst alternative.

Declaration of competing interest

The authors declare that they have no known competing financial interests or personal relationships that could have appeared to influence the work reported in this paper.

Appendix A. Supplementary data

Supplementary data to this article can be found online at https://doi.org/10.1016/j.ijhydene.2021.06.088.

REFERENCES

[1] Godula-Jopek A, Millet P, Guillet N, Laurencin J, Mougin J, Bourasseau C, et al. Hydrogen production by electrolysis. Weinheim: Wiley-VCH Verlag GmbH & Co. KGaA; 2015.

[2] Fabbri E, Schmidt TJ. Oxygen evolution reaction—the enigma in water electrolysis. ACS Catal 2018;8:9765–74. https://doi.org/10.1021/acscatal.8b02712.

[3] Li Z, Lv L, Ao X, Li JG, Sun H, An P, et al. An effective method for enhancing oxygen evolution kinetics of LaMO3 (M = Ni, Co, Mn) perovskite catalysts and its application to a rechargeable zinc–air battery. Appl Catal B Environ 2020;262. https://doi.org/10.1016/j.apcatb.2019.118291.

[4] Yu L, Xu N, Zhu T, Xu Z, Sun M, Geng D. La0.4Sr0.6Co0.7Fe0.2Nb0.1O3-δ perovskite prepared by the sol-gel method with superior performance as a bifunctional oxygen electrocatalyst. Int J Hydrogen Energy 2020;45:30583–91. https://doi.org/10.1016/j.ijhydene.2020.08.105.

[5] Hegde GS, Ghosh A, Badam R, Matsumi N, Sundara R. Role of defects in low-cost perovskite catalysts toward ORR and OER in lithium-oxygen batteries. ACS Appl Energy Mater 2020;3(2):1338–48. https://doi.org/10.1021/acsaem.9b01727.

[6] Omari E, Omari M. Cu-doped GdFeO3 perovskites as electrocatalysts for the oxygen evolution reaction in alkaline media. Int J Hydrogen Energy 2019;44:28769–79. https://doi.org/10.1016/j.ijhydene.2019.09.088.

[7] Hao Z, Wei P, Yang Y, Sun J, Song Y, Guo D, et al. Self-assembled CuCo2S4 nanosheets with rich surface Co3+ as efficient electrocatalysts for oxygen evolution reaction. Appl Surf Sci 2021;536:147826. https://doi.org/10.1016/j.apsusc.2020.147826.

[8] Xiong P, Yang F, Ding Z, Jia Y, Liu J, Yan X, et al. Preparation and electrocatalytic properties of spinel CoxFe3-xO4 nanoparticles. Int J Hydrogen Energy 2020;45:13841–7. https://doi.org/10.1016/j.ijhydene.2020.03.098.

[9] Peng X, wang zhao. Facile route of P-doped defect-rich manganese-cobalt oxide spinel with enhanced oxygen evolution reaction performance. ChemNanoMat 2020;6(12):1812–8. https://doi.org/10.1002/cnma.202000475.

[10] Lankauf K, Cysewska K, Karczewski J, Mielewczyk-Gryń A, Górnicka K, Cempura G, et al. MnxCo3-xO4 spinel oxides as efficient oxygen evolution reaction catalysts in alkaline media. Int J Hydrogen Energy 2020;5. https://doi.org/10.1016/j.ijhydene.2020.03.188.

[11] Wang P, Qin R, Ji P, Pu Z, Zhu J, Lin C, et al. Synergistic coupling of Ni nanoparticles with Ni3C nanosheets for highly

efficient overall water splitting. Small 2020;16:1–10. https://doi.org/10.1002/smll.202001642.

[12] Zakaria MB, Zheng D, Apfel UP, Nagata T, Kenawy ERS, Lin J. Dual-heteroatom-doped reduced graphene oxide sheets conjoined CoNi-based carbide and sulfide nanoparticles for efficient oxygen evolution reaction. ACS Appl Mater Interfaces 2020;12:40186–93. https://doi.org/10.1021/acsami.0c06141.

[13] Zhu S, Lei J, Zhang L, Lu L. Efficient electrocatalytic oxygen evolution by Fe3C nanosheets perpendicularly grown on 3D Ni foams. Int J Hydrogen Energy 2019;44:16507–15. https://doi.org/10.1016/j.ijhydene.2019.04.214.

[14] Li Y, Ge L, Zhou Y, Li L, Li W, Xu J, et al. KB-templated, in situ synthesis of highly dispersed bimetallic NiFe phosphides as efficient oxygen evolution catalysts. Inorg Chem Front 2020;7:4930–8. https://doi.org/10.1039/D0QI00627K.

[15] Zhang Y, Xu J, Ding Y, Wang C. Tuning the d-band center enables nickel-iron phosphide nanoprisms as efficient electrocatalyst towards oxygen evolution. Int J Hydrogen Energy 2020;45:17388–97. https://doi.org/10.1016/j.ijhydene.2020.04.213.

[16] Xie Y, Chen M, Cai M, Teng J, Huang H, Fan Y, et al. Hollow cobalt phosphide with N-doped carbon skeleton as bifunctional electrocatalyst for overall water splitting. Inorg Chem 2019;58:14652–9. https://doi.org/10.1021/acs.inorgchem.9b02333.

[17] Karmakar A, Karthick K, Kumaravel S, Sankar SS, Kundu S. Enabling and inducing oxygen vacancies in cobalt iron layer double hydroxide via selenization as precatalysts for electrocatalytic hydrogen and oxygen evolution reactions. Inorg Chem 2021;60(3):2023–36. https://doi.org/10.1021/acs.inorgchem.0c03514.

[18] Ma G, Du X, Zhang X. Facile synthesis of molybdenum-based layered double hydroxide nanorods for boosting water oxidation reaction. Int J Hydrogen Energy 2020;45(58):33641–7. https://doi.org/10.1016/j.ijhydene.2020.09.097.

[19] Cysewska K, Rybarczyk MK, Cempura G, Jasinski P, Molin S. The influence of the electrodeposition parameters on the properties of Mn-Co-based nanofilms as anode materials for alkaline electrolysers. Materials 2020;13. https://doi.org/10.3390/ma13112662.

[20] Antipin D, Risch M. Trends of epitaxial perovskite oxide films catalyzing the oxygen evolution reaction in alkaline media. J Phys Energy 2020;2:032003. https://doi.org/10.1088/2515-7655/ab812f.

[21] Suntivich J, May KJ, Gasteiger HA, Goodenough JB, Shao-Horn Y. A perovskite oxide optimized for oxygen evolution catalysis from molecular orbital principles. Science 2011;334:1383–5. https://doi.org/10.1126/science.1212858. 80-.

[22] Tasleem S, Tahir M. Recent progress in structural development and band engineering of perovskites materials for photocatalytic solar hydrogen production: a review. Int J Hydrogen Energy 2020;45:19078–111. https://doi.org/10.1016/j.ijhydene.2020.05.090.

[23] Zhang Z, Zhou D, Wu X, Bao X, Liao J, Wen M. Synthesis of La 0.2 Sr 0.8 CoO 3 and its electrocatalytic activity for oxygen evolution reaction in alkaline solution. Int J Hydrogen Energy 2019;44:7222–7. https://doi.org/10.1016/j.ijhydene.2019.01.268.

[24] Deng H, Shu L, Wang Z, Mao J, Liang F. SrTi0.1CoxFe0.9-xO3-δ Perovskites for enhanced oxygen evolution reaction activity. Int J Hydrogen Energy 2020;45:13129–38. https://doi.org/10.1016/j.ijhydene.2020.03.057.

[25] Zhang SL, Cox D, Yang H, Park BK, Li CX, Li CJ, et al. High stability SrTi1-: XFexO3-δ electrodes for oxygen reduction and oxygen evolution reactions. J Mater Chem 2019;7:21447–58. https://doi.org/10.1039/c9ta07548h.

[26] Zhang S, Wang H, Yang T, Lu MY, Li C, Li C, et al. Advanced oxygen-electrode-supported solid oxide electrochemical cells with Sr(Ti,Fe)O3-δ-based fuel electrodes for electricity generation and hydrogen production. J Mater Chem 2020;8:25867–79. https://doi.org/10.1039/d0ta06678h.

[27] Shah MAKY, Rauf S, Mushtaq N, Tayyab Z, Ali N, Yousaf M, et al. Semiconductor Fe-doped SrTiO3-δ perovskite electrolyte for low-temperature solid oxide fuel cell (LT-SOFC) operating below 520 °C. Int J Hydrogen Energy 2020;45:14470–9. https://doi.org/10.1016/j.ijhydene.2020.03.147.

[28] Kamran Yousaf Shah MA, Mushtaq N, Rauf S, Xia C, Zhu B. The semiconductor SrFe0.2Ti0.8O3-δ-ZnO heterostructure electrolyte fuel cells. Int J Hydrogen Energy 2019;44:30319–27. https://doi.org/10.1016/j.ijhydene.2019.09.145.

[29] Zhuang Y, Lin Y, Zhu D, Zheng Y, Yu Z. A study of conductivity in the Sr(Fe1−xTix)O3−δ system. J Am Ceram Soc 1989;72:1444–6. https://doi.org/10.1111/j.1151-2916.1989.tb07671.x.

[30] Kharton VV, Kovalevsky AV, Tsipis EV, Viskup AP, Naumovich EN, Jurado JR, et al. Mixed conductivity and stability of A-site-deficient Sr(Fe,Ti)O 3-δ perovskites. J Solid State Electrochem 2002;7:30–6. https://doi.org/10.1007/s10008-002-0286-3.

[31] Galakhov VR, Kurmaev EZ, Kuepper K, Neumann M, McLeod JA, Moewes A, et al. Valence band structure and X-ray spectra of oxygen-deficient ferrites SrFeOx. J Phys Chem C 2010;114:5154–9. https://doi.org/10.1021/jp909091s.

[32] Rothschild A, Menesklou W, Tuller HL, Ivers-Tiffée E. Electronic structure, defect chemistry, and transport properties of SrTi 1-xFe xO 3-y solid solutions. Chem Mater 2006;18:3651–9. https://doi.org/10.1021/cm052803x.

[33] Litzelman SJ, Rothschild A, Tuller HL. The electrical properties and stability of SrTi0.65Fe0.35O3−δ thin films for automotive oxygen sensor applications. Sensor Actuator B Chem 2005;108:231–7. https://doi.org/10.1016/j.snb.2004.10.040.

[34] Hayden BE, Rogers FK. Oxygen reduction and oxygen evolution on SrTi1 − xFexO3 − y (STFO) perovskite electrocatalysts. J Electroanal Chem 2018;819:275–82. https://doi.org/10.1016/j.jelechem.2017.10.056.

[35] Mroziński A, Molin S, Karczewski J, Miruszewski T, Jasiński P. Electrochemical properties of porous Sr 0.86 Ti 0.65 Fe 0.35 O 3 oxygen electrodes in solid oxide cells: impedance study of symmetrical electrodes. Int J Hydrogen Energy 2019;44:1827–38. https://doi.org/10.1016/j.ijhydene.2018.11.203.

[36] Mroziński A, Molin S, Karczewski J, Kamecki B, Jasiński P. The influence of iron doping on performance of SrTi. ECS Trans 2019;91:1299–307. https://doi.org/10.1149/09101.1299ecst.

[37] Mroziński A, Molin S, Jasiński P. Study of oxygen electrode reactions on symmetrical porous SrTi0.30Fe0.70O3-δ electrodes on Ce0.8Gd0.2O1.9 electrolyte at 800 °C–500 °C. Electrochim Acta 2020:346. https://doi.org/10.1016/j.electacta.2020.136285.

[38] Schneider CA, Rasband WS, Eliceiri KW. NIH Image to ImageJ: 25 years of image analysis. Nat Methods 2012;9:671–5. https://doi.org/10.1038/nmeth.2089.

[39] Rodriguez-Carvajal J. Recent advances in magnetic structure determination by neutron powder diffraction. Phys B 1993;55–69. https://doi.org/10.1016/0921-4526(93)90108-I.

[40] Adler P, Eriksson S. Structural properties, Mössbauer spectra, and magnetism of perovskite-type oxides SrFe1-xTixO3-y. Zeitschrift Fur Anorg Und Allg Chemie 2000;626:118–24. https://doi.org/10.1002/(sici)1521-3749(200001)626:1<118::aid-zaac118>3.0.co;2-k.

[41] Blasco J, Stankiewicz J, García J. Phase segregation in the Gd1-xSrxFeO 3-δ series. J Solid State Chem 2006;179:898–908. https://doi.org/10.1016/j.jssc.2005.12.023.

[42] VAN DER Pauw LJ. A method of measuring the resistivity and Hall coefficient on lamellae of arbitrary shape. Philips Tech Rev 1958;20:220–4.

[43] Suntivich J, Gasteiger HA, Yabuuchi N, Shao-Horn Y. Electrocatalytic measurement methodology of oxide catalysts using a thin-film rotating disk electrode. J Electrochem Soc 2010;157:B1263. https://doi.org/10.1149/1.3456630.

[44] Yagi S, Yamada I, Tsukasaki H, Seno A, Murakami M, Fujii H, et al. Covalency-reinforced oxygen evolution reaction catalyst. Nat Commun 2015;6:1–6. https://doi.org/10.1038/ncomms9249.

[45] Garsany Y, Ge J, St-Pierre J, Rocheleau R, Swider-Lyons KE. Analytical procedure for accurate comparison of rotating disk electrode results for the oxygen reduction activity of Pt/C. J Electrochem Soc 2014;161:628–40. https://doi.org/10.1149/2.036405jes.

[46] Alia SM, Pivovar BS. Evaluating hydrogen evolution and oxidation in alkaline media to establish baselines. J Electrochem Soc 2018;165:F441–55. https://doi.org/10.1149/2.0361807jes.

[47] McCrory CCL, Jung S, Peters JC, Jaramillo TF. Benchmarking heterogeneous electrocatalysts for the oxygen evolution reaction. J Am Chem Soc 2013;135:16977–87. https://doi.org/10.1021/ja407115p.

[48] Wei C, Rao RR, Peng J, Huang B, Stephens IEL, Risch M, et al. Recommended practices and benchmark activity for hydrogen and oxygen electrocatalysis in water splitting and fuel cells. Adv Mater 2019;1806296:1–24. https://doi.org/10.1002/adma.201806296.

[49] Schulze-Küppers F, Ten Donkelaar SFP, Baumann S, Prigorodov P, Sohn YJ, Bouwmeester HJM, et al. Structural and functional properties of SrTi1-xFexO3-δ (0 ≤ x ≤ 1) for the use as oxygen transport membrane. Separ Purif Technol 2015;147:414–21. https://doi.org/10.1016/j.seppur.2014.12.020.

[50] Fabbri E, Nachtegaal M, Binninger T, Cheng X, Kim B-J, Durst J, et al. Dynamic surface self-reconstruction is the key of highly active perovskite nano-electrocatalysts for water splitting. Nat Mater 2017;1–8. https://doi.org/10.1038/nmat4938.

[51] Su C, Wang W, Chen Y, Yang G, Xu X, Tadé MO, et al. SrCo0.9Ti0.1O3-δ as a new electrocatalyst for the oxygen evolution reaction in alkaline electrolyte with stable performance. ACS Appl Mater Interfaces 2015;7:17663–70. https://doi.org/10.1021/acsami.5b02810.

[52] Zhu Y, Zhou W, Chen ZG, Chen Y, Su C, Tadé MO, et al. SrNb0.1Co0.7Fe0.2O3-δ perovskite as a next-generation electrocatalyst for oxygen evolution in alkaline solution. Angew Chem Int Ed 2015;54:3897–901. https://doi.org/10.1002/anie.201408998.

[53] Cheng X, Fabbri E, Kim B, Nachtegaal M, Schmidt TJ. Effect of ball milling on the electrocatalytic activity of Ba0.5Sr0.5Co0.8Fe0.2O3 towards the oxygen evolution reaction. J Mater Chem 2017;5:13130–7. https://doi.org/10.1039/c7ta00794a.

[54] Zhang H, Guan D, Gao X, Yu J, Chen G, Zhou W, et al. Morphology, crystal structure and electronic state one-step co-tuning strategy towards developing superior perovskite electrocatalysts for water oxidation. J Mater Chem 2019;7:19228–33. https://doi.org/10.1039/c9ta06020k.

[55] Longo VM, Das Graça Sampaio Costa M, Zirpole Simões A, Rosa ILV, Santos COP, Andrés J, et al. On the photoluminescence behavior of samarium-doped strontium titanate nanostructures under UV light. A

structural and electronic understanding. Phys Chem Chem Phys 2010;12:7566–79. https://doi.org/10.1039/b923281h.

[56] Kim CS, Bishop SR, Perry NH, Tuller HL. Electro-chemo-mechanical studies of perovskite-structured mixed ionic-electronic conducting SrSn1-xFexO3-x/2+δpart I: defect chemistry. J Electroceram 2017;38:74–80. https://doi.org/10.1007/s10832-017-0064-3.

[57] Filatova EO, Egorova YV, Galdina KA, Scherb T, Schumacher G, Bouwmeester HJM, et al. Effect of Fe content on atomic and electronic structure of complex oxides Sr(Ti,Fe)O3 − δ. Solid State Ionics 2017;308:27–33. https://doi.org/10.1016/j.ssi.2017.05.016.

[58] Badreldin A, Abusrafa AE, Abdel-Wahab A. Oxygen-deficient perovskites for oxygen evolution reaction in alkaline media: a review. Emergent Mater 2020;3:567–90. https://doi.org/10.1007/s42247-020-00123-z.

[59] Chatzichristodoulou C, Norby P, Hendriksen PV, Mogensen MB. Size of oxide vacancies in fluorite and perovskite structured oxides. J Electroceram 2015;34:100–7. https://doi.org/10.1007/s10832-014-9916-2.

[60] Falcón H, Barbero JA, Alonso JA, Martínez-Lope MJ, Fierro JLG. SrFeO3-δ perovskite oxides: chemical features and performance for methane combustion. Chem Mater 2002;14:2325–33. https://doi.org/10.1021/cm011292l.

[61] Steinsvik S, Bugge R, Gjønnes J, Taftø J, Norby T. The defect structure of SrTi 1−x Fe x O 3−y (x = 0−0.8) investigated by electrical cdoncutivity measurements and electron energy loss spectroscopy (EELS). J Phys Chem Solid 1997;58:969–76. https://doi.org/10.1016/S0022-3697(96)00200-4.

[62] Miruszewski T, Dzierzgowski K, Winiarz P, Wachowski S, Mielewczyk-Gryń A, Gazda M. Structural properties and water uptake of STi1-xFexO3-x/2-δ. Materials 2020;13. https://doi.org/10.3390/ma13040965.

[63] Koo B, Kim K, Kim JK, Kwon H, Han JW, Jung WC. Sr segregation in perovskite oxides: why it happens and how it exists. Joule 2018;2:1476–99. https://doi.org/10.1016/j.joule.2018.07.016.

[64] Nenning A, Opitz AK, Rameshan C, Rameshan R, Blume R, Hävecker M, et al. Ambient pressure XPS study of mixed conducting perovskite-type SOFC cathode and anode materials under well-defined electrochemical polarization. J Phys Chem C 2016;120:1461–71. https://doi.org/10.1021/acs.jpcc.5b08596.

[65] Boucly A, Fabbri E, Artiglia L, Cheng X, Pergolesi D, Ammann M, et al. Surface segregation acts as surface engineering for the oxygen evolution reaction on perovskite oxides in alkaline media. Chem Mater 2020;32:5256–63. https://doi.org/10.1021/acs.chemmater.0c01396.

[66] Ghaffari M, Shannon M, Hui H, Tan OK, Irannejad A. Preparation, surface state and band structure studies of SrTi(1-X)Fe(x)O (3-δ) (x = 0-1) perovskite-type nano structure by X-ray and ultraviolet photoelectron spectroscopy. Surf Sci 2012;606:670–7. https://doi.org/10.1016/j.susc.2011.12.013.

[67] Fetisov AV, Kozhina GA, Estemirova SK, Fetisov VB, Gulyaeva RI. XPS study of the chemical stability of DyBa2Cu3O6+δ superconductor. Phys C Supercond Its Appl 2015;508:62–8. https://doi.org/10.1016/j.physc.2014.11.003.

[68] Zhu J, Li H, Zhong L, Xiao P, Xu X, Yang X, et al. Perovskite oxides: preparation, characterizations, and applications in heterogeneous catalysis. ACS Catal 2014;4:2917–40. https://doi.org/10.1021/cs500606g.

[69] Torrance JB, Lacorro P, Asavaroengchai C, Metzger RM. Simple and perovskite oxides of transition-metals: why some are metallic, while most are insulating. J Solid State Chem 1991;90:168–72. https://doi.org/10.1016/0022-4596(91)90182-H.

[70] Kuhn M, Kim JJ, Bishop SR, Tuller HL. Oxygen nonstoichiometry and defect chemistry of perovskite-

structured BaxSr1-xTi1-yFeyO 3-y/2+δ solid solutions. Chem Mater 2013;25:2970–5. https://doi.org/10.1021/cm400546z.

[71] Perry NH, Kim JJ, Bishop SR, Tuller HL. Strongly coupled thermal and chemical expansion in the perovskite oxide system Sr(Ti,Fe)O3-α. J Mater Chem 2015;3:3602–11. https://doi.org/10.1039/c4ta05247a.

[72] Fabbri E, Nachtegaal M, Cheng X, Schmidt TJ. Superior bifunctional electrocatalytic activity of Ba0.5Sr0.5Co0.8Fe0.2O3-δ/Carbon composite electrodes: insight into the local electronic structure. Adv Energy Mater 2015;5:1–5. https://doi.org/10.1002/aenm.201402033.

[73] Wang H, Zhou M, Choudhury P, Luo H. Perovskite oxides as bifunctional oxygen electrocatalysts for oxygen evolution/reduction reactions − a mini review. Appl Mater Today 2019;16:56–71. https://doi.org/10.1016/j.apmt.2019.05.004.

[74] Kamecki B, Karczewski J, Abdoli H, Chen M, Jasiński G, Jasiński P, et al. Deposition and electrical and structural properties of La0.6Sr0.4CoO3 thin films for application in high-temperature electrochemical cells. J Electron Mater 2019;48:5428–41. https://doi.org/10.1007/s11664-019-07372-7.

[75] Vogt UF, Sfeir J, Richter J, Soltmann C, Holtappels P. B-site substituted lanthanum strontium ferrites as electrode materials for electrochemical applications. Pure Appl Chem 2008;80:2543–52. https://doi.org/10.1351/pac200880112543.

[76] Schmidt TJ, Marzari N, El Kazzi M, Haumont R, Castelli IE, Fabbri E, et al. Oxygen evolution reaction on La 1− x Sr x CoO 3 perovskites: a combined experimental and theoretical study of their structural, electronic, and electrochemical properties. Chem Mater 2015;27:7662–72. https://doi.org/10.1021/acs.chemmater.5b03138.

[77] Hirai S, Ohno T, Uemura R, Maruyama T, Furunaka M, Fukunaga R, et al. Ca1-xSrxRuO3 perovskite at the metal-insulator boundary as a highly active oxygen evolution catalyst. J Mater Chem 2019;7:15387–94. https://doi.org/10.1039/c9ta03789f.

[78] Practices B, Performance RE. Best practices for reporting electrocatalytic performance of nanomaterials. 2018. p. 10–3. https://doi.org/10.1021/acsnano.8b07700.

[79] Liu Y, Yin S, Shen PK. Asymmetric 3d electronic structure for enhanced oxygen evolution catalysis. ACS Appl Mater Interfaces 2018;10:23131–9. https://doi.org/10.1021/acsami.8b06106.

[80] Bhowmick S, Dhankhar A, Sahu TK, Jena R, Gogoi D, Peela NR, et al. Low overpotential and stable electrocatalytic oxygen evolution reaction utilizing doped perovskite oxide, La 0.7 Sr 0.3 MnO 3 , modified by cobalt phosphate. ACS Appl Energy Mater 2020;3(2):1279–85. https://doi.org/10.1021/acsaem.9b02167.

[81] Lin Q, Zhu Y, Hu Z, Yin Y, Lin HJ, Chen C Te, et al. Boosting the oxygen evolution catalytic performance of perovskites: via optimizing calcination temperature. J Mater Chem 2020;8:6480–6. https://doi.org/10.1039/c9ta13972a.

[82] Baumung M, Schönewald F, Erichsen T, Volkert CA, Risch M. Influence of particle size on the apparent electrocatalytic

activity of LiMn2O4 for oxygen evolution. Sustain Energy Fuels 2019;3:2218–26. https://doi.org/10.1039/c8se00551f.

[83] Xu S, Wang M, Saranya G, Chen N, Zhang L, He Y, et al. Pressure-driven catalyst synthesis of Co-doped Fe3C@Carbon nano-onions for efficient oxygen evolution reaction. Appl Catal B Environ 2020;268:118385. https://doi.org/10.1016/j.apcatb.2019.118385.

[84] Shen Z, Zhuang Y, Li W, Huang X, Oropeza FE, Hensen EJM, et al. Increased activity in the oxygen evolution reaction by Fe 4+ -induced hole states in perovskite La 1−x Sr x FeO 3. J Mater Chem 2020:4407–15. https://doi.org/10.1039/c9ta13313e.

[85] Song S, Zhou J, Sun J, Zhang S, Lin X, Hu Z, et al. Understanding the origin of high oxygen evolution reaction activity in the high Sr-doped perovskite. Chin J Catal 2020;41:592–7. https://doi.org/10.1016/S1872-2067(19)63441-8.

[86] Doyle RL, Godwin IJ, Brandon MP, Lyons MEG. Redox and electrochemical water splitting catalytic properties of hydrated metal oxide modified electrodes. Phys Chem Chem Phys 2013;15:13737–83. https://doi.org/10.1039/c3cp51213d.

[87] Lu Y, Ma A, Yu Y, Tan R, Liu C, Zhang P, et al. Engineering oxygen vacancies into LaCoO 3 perovskite for efficient electrocatalytic oxygen evolution. ACS Sustainable Chem Eng 2019;7:2906–10. https://doi.org/10.1021/acssuschemeng.8b05717.

[88] Hona RK, Ramezanipour F. Effect of the oxygen vacancies and structural order on the oxygen evolution activity: a case study of SrMnO3-δ featuring four different structure types. Inorg Chem 2020;59:4685–92. https://doi.org/10.1021/acs.inorgchem.9b03774.

[89] She S, Yu J, Tang W, Zhu Y, Chen Y, Sunarso J, et al. Systematic study of oxygen evolution activity and stability on La 1− x Sr x FeO 3−δ perovskite electrocatalysts in alkaline media. ACS Appl Mater Interfaces 2018;10:11715–21. https://doi.org/10.1021/acsami.8b00682.

[90] Pan Y, Xu X, Guan D, Hayre RO, Shao Z, Zhong Y, et al. Direct evidence of boosted oxygen evolution over perovskite by enhanced lattice oxygen participation. Nat Commun 2020:1–10. https://doi.org/10.1038/s41467-020-15873-x.

[91] Shinagawa T, Garcia-Esparza AT, Takanabe K. Insight on Tafel slopes from a microkinetic analysis of aqueous electrocatalysis for energy conversion. Sci Rep 2015;5:1–21. https://doi.org/10.1038/srep13801.

[92] Zhu Y, Tahini HA, Hu Z, Chen Z, Zhou W, Komarek AC, et al. Boosting oxygen evolution reaction by creating both metal ion and lattice-oxygen active sites in a complex oxide. 2019. p. 1–8. https://doi.org/10.1002/adma.201905025. 1905025.

[93] Yu J, Yu J, Wu X, Guan D, Hu Z, Weng SC, et al. Monoclinic SrIrO3: an easily synthesized conductive perovskite oxide with outstanding performance for overall water splitting in alkaline solution. Chem Mater 2020;32:4509–17. https://doi.org/10.1021/acs.chemmater.0c00149.